ARTICLE NO. 80-4053

A80-042

Ballistic Missile Re-entry Dispersion

20017
40002
40005

Hartley H. King*
Effects Technology, Inc., Santa Barbara, Calif.

In this paper two important sources of re-entry trajectory dispersion are described: that due to frustum boundary-layer transition, and that due to separated flow on the indented nosetip which may occur after nosetip transition. For both phenomena, incremental lateral forces are estimated, and the effect of these forces on dispersion is evaluated. Vehicle design approaches for minimizing dispersion from these sources are given.

Nomenclature

A = complex angle of attack = $(\dot{\bar{y}}_2 + i\dot{\bar{y}}_3)/u_0$
B = complex body axis orientation (Fig. 1)
$C_{M\alpha}$ = $dC_M/d\alpha$, C_M = c.g. moment/$\bar{q}SL$
$C_{N\alpha}$ = $dC_N/d\alpha$, C_N = normal force/$\bar{q}S$
C_{Mq} = $dC_M/d(qL/u_0)$
C_{Nq} = $dC_N/d(qL/u_0)$
C_{FB} = body-fixed force coefficient
C_{MB} = body-fixed moment coefficient (about c.g.)
C_X = axial force/$\bar{q}S$
h = altitude
I, I_x = pitch and roll inertia, respectively
K = parameter group, Eq. (3)
k = roughness height
L = reference length (stagnation point to base)
m = mass
P = pressure
p = roll rate
q,r = pitch and yaw rates, respectively (about y_2, y_3)
$\bar{q}$ = dynamic pressure = $\rho u_0^2/2$
r_n, r_b = nose and base radius, respectively
S = reference area (base area)
s = streamlength
t = time
u_0 = axial velocity
V = lateral velocity = $(A+B)u_0$
x = axial length behind stagnation point
α = angle of attack
γ = flight path angle (+ down)
Δ = incremental change
δ^* = boundary-layer displacement thickness
η = angle relative to body reference y_2
ρ = density
τ = shear stress
Φ = angle relative to horizontal $\bar{y}_2$

Superscripts

$(\dot{\ })$ = time derivative = d/dt
$(\tilde{\ })$ = in nonrolling axis system
$(\ )'$ = nondimensional time derivative = $(L/u_0)d/dt$

Subscripts

ac = aerodynamic center
cg = center of gravity
e = at entry altitude (100 km)
s = static margin

Received April 24, 1979; revision received Oct. 29, 1979.

Index categories: LV/M Aerodynamics; LV/M Dynamics and Control; Supersonic and Hypersonic Flow.

*Research Specialist. Member AIAA.

Introduction

WITH continued improvements in launch system performance, trajectory dispersion during re-entry has become an important component of the ballistic missile system error budget. In addition to survival, the re-entry vehicle design process must consider accuracy. Thus, there is a need to identify and model all of the dispersive mechanisms in order to make a quantitative design optimization.

For typical ICBM trajectories natural variations in atmospheric wind and density profiles produce impact point uncertainties of 20-50 m for high ballistic coefficient vehicles.[1] Thus a design goal is to reduce other dispersion sources to these levels. Presently, the largest sources of targeting error are associated with laminar-to-turbulent boundary-layer transition on the vehicle.[2,3] With transition on the cone frustum, the greater induced pressure and skin friction of the turbulent boundary layer, as compared to laminar, can produce significant lateral forces from transition pattern asymmetry. After progression to the nosetip, transition increases the ablation rate downstream of the stagnation point and may produce a concave shape sufficiently indented to cause flow separation.[4,5] Separation suddenly changes the effective nosetip shape and vehicle lateral forces. Other potential dispersion sources include heatshield roll torque,[6] erosion from atmospheric water or ice that tends to blunt the tip and cause shortfall, and other discrete aerodynamic events such as the removal of protective covering devices.

This paper attempts to describe and evaluate the significance to re-entry accuracy of both the frustum transition and nosetip separation dispersion mechanisms. The object is to describe the relevant fluid mechanical phenomenology and present numerical estimates of various quantities which relate to trajectory dispersion. In this way the influence on dispersion of vehicle and trajectory parameters is explained. The paper is arranged in three main parts. The first discusses vehicle lateral motion and indicates how changes in lateral forces can lead to permanent trajectory deflection; the second describes the forcing functions and motions associated with frustum transition; and the third shows the potential severity of nosetip separation as a source of dispersion.

Motion Analysis

The response of a vehicle to changes in lateral forces is described by Platus[7] and Crenshaw,[8] and several types of dispersion producing aerodynamic forcing fucntions are identified. Probably the most important of these is a change in body-fixed lateral force (i.e., trim force) on a time scale shorter than the precession period. A second type described by Platus is a wind plane (wind fixed) incremental force that is large enough to destabilize the vehicle for a short time.

In this section the significant features of the motion analysis leading to the dispersion equation are reviewed. The

method described here includes the explicit coupling of the lateral and angular motion. It yields an expression for dispersion due to step trim changes that is different from that of Refs. 7 and 8 in that the significant moment axis is the aerodynamic center location rather than the center of gravity.

For the small trajectory perturbations of interest here the axial motion is essentially ballistic, and the lateral motion is adequately described by a small angle analysis. The solution for the motion response closely follows that of Ref. 9 and is fully presented in Ref. 10. Thus only a brief outline of the derivation and the main results are given. From the lateral motion solution, the impact point dispersion due to a force change event may be estimated by projecting to impact altitude the mean flight path angle deviation.

The equations of motion of a roll symmetric vehicle are expressed in a nonrolling body-fixed coordiante system $\tilde{y}$ which has its $\tilde{y}_1$ axis aligned with the body-fixed rolling coordinate system y_1 (Fig. 1). The orientation of the vehicle is given by the angle B of axis y_1, with respect to a space-fixed system x. Complex variable notation is employed here for brevity, but the component equations of motion are integrated numerically for the motion results presented later. The equations are

$$m\dot{V}=\bar{q}S[-C_{N\alpha}A+C_{Nq}B'+C_{FB}e^{i(\Phi+\eta_{FB})}] \quad (1a)$$

$$I\ddot{B}-iI_x p\dot{B}=\bar{q}SL[-C_{M\alpha}A+C_{Mq}B'-iC_{MB}e^{i(\Phi+\eta_{MB})}] \quad (1b)$$

For the case of constant coefficients, Eqs. (1) can be solved in closed form using Laplace transforms.[9,10] The results for $A(t)$, $B(t)$, and $V(t)$ then assume the form of "tricyclic" equations. For example, the lateral velocity has the form

$$V(t)=V_1e^{\lambda_1 t}+V_2e^{\lambda_2 t}+V_3e^{ipt}+V_4 \quad (2)$$

where the V_i are constants and the λ_j are characteristic roots. The first three terms are periodic, so the V_4 term defines the mean direction of motion. The vectorial mean direction change $\Delta\vec{V}$ due to a step change in body-fixed forces is derivable from the change in V_4. For the simple case where $\eta_{MB}=\eta_{FB}+\pi/2$ (effectively a single lateral force), the velocity change magnitude is approximately[10]

$$\Delta V=K\Delta C_{MBac} \qquad K\equiv\frac{\rho u_0^2 SL}{2mp\Delta x_s} \quad (3)$$

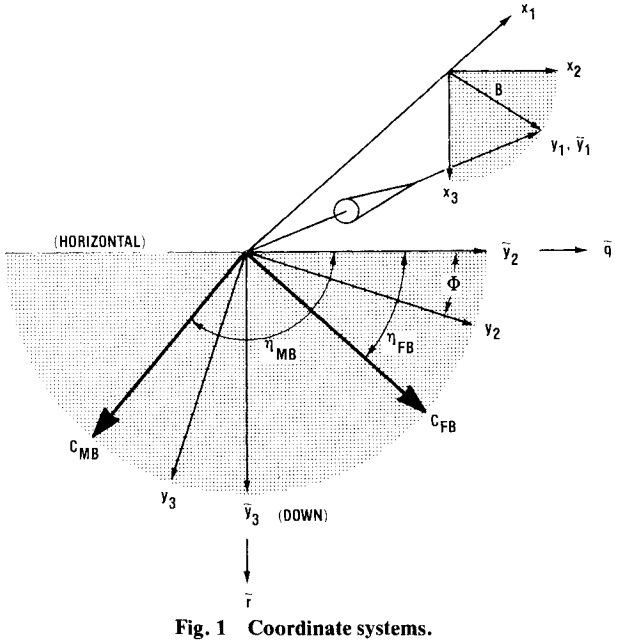

Fig. 1 Coordinate systems.

A more complicated expression is required when the moment vector does not lead the force by $\pi/2$.[10] Equation (3) has the same form as that of Platus and Crenshaw except that the relevant moment axis is at the aerodynamic center. For an impulsive lateral force, the mean velocity jump magnitude is obtained in the same manner:

$$\Delta V=\frac{\rho u_0^2 SL}{2m\Delta x_s}\int_{\Delta t-0}\Delta C_{Mac}\,dt \quad (4)$$

This gives the velocity change when the time of force application is short compared to the roll or precession period. Mean dispersion normal to the trajectory at zero altitude then can be estimated from

$$\Delta r=h\Delta V/(u_0\sin\gamma) \quad (5)$$

for a velocity jump event occurring at altitude h.

Frustum Transition

The object of this section is to describe the frustum transition dispersion mechanism for a typical vehicle, a sphere-cone with a carbon-carbon nosetip and low blowing rate heat shield material such as carbon phenolic. Numerical estimates of incremental forces and trajectory response are obtained for two example vehicles flying a ballistic trajectory. The idea is to examine the factors which cause transition pattern asymmetry and see how these lead to dispersion. Relevant vehicle parameters, trajectory, and aerodynamic data[11,12] needed for this analysis are given in Table 1.

Symmetric Progression

For a symmetric body at zero angle of attack, transition ideally progresses forward symmetrically during descent. Berkowitz, Kyriss, and Martellucci[13] (BKM) attempted to obtain a flight vehicle transition correlation which approached this condition. They found that local edge momentum thickness Reynolds number Re_θ vs axial distance ratio x/r_n best collapsed the start of transition data from some seventy vehicles. The data are indicated by the shaded area in Fig. 2. The scatter is attributed to different nosetip and heat shield materials and to surface roughness.[13]

Table 1 Typical vehicle and trajectory parameters

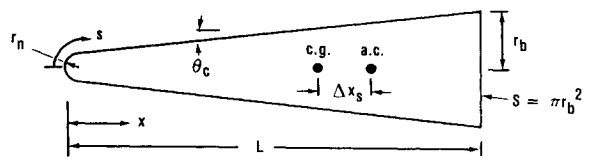

	Sharp	Blunt
Nose radius r_n, cm	2.0	4.0
Bluntness r_n/r_b	0.074	0.147
Cone half-angle θ_c, deg	8.0	7.5
Vehicle length L, cm	180	180
Base area S, cm^2	2296	2325
Mass m, kg	160	160
Pitch inertia I, kg-m^2	35	35
Roll inertia I_x, kg-m^2	3.5	3.5
Center of gravity x_{cg}/L	0.605	0.66
Static margin $\Delta x_s/L$	0.067	0.067
Normal force slope $C_{N\alpha}$, deg^{-1}	0.0371	0.0273
C.g. moment slope $C_{M\alpha}$, deg^{-1}	−0.00230	−0.001829
Damping coef. C_{Nq}	0.11	−0.04
Damping coef. C_{Mq}	−0.13	−0.14
Ballistic coef. m/C_xS, kg/m^2	13,400	10,120
Entry velocity u_e, km/s	7.2	7.2
Entry angle γ_e, deg	30	30
Entry roll rate p_e, deg/s	360	360

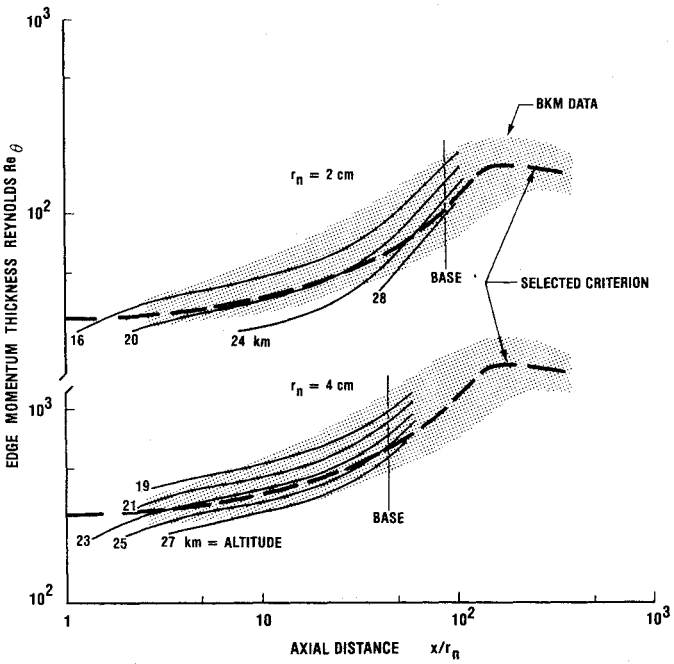

Fig. 2 Symmetric transition progression.

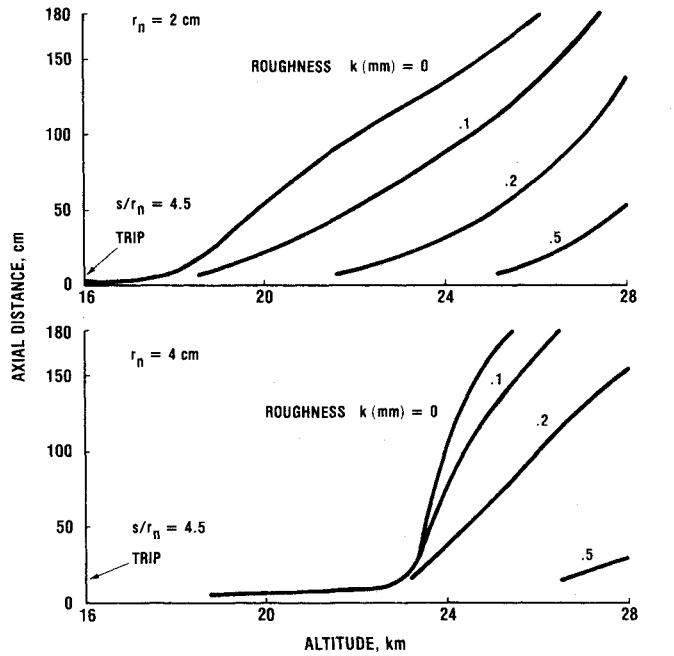

Fig. 3 Roughness effect on transition progression.

Asymmetric patterns customarily are referenced to the symmetric transition progression, so it is useful to estimate this for the example vehicles of Table 1. Reference 14 describes the boundary-layer analysis used to obtain the Re_θ curves shown in Fig. 2 and the incremental transition pattern forces given later. The analysis is a momentum integral approach which uses real air thermal properties and includes entropy layer swallowing effects on the boundary layer edge conditions. Wall temperature is assumed to be 3500 K on the nose and 1200 K on the frustum. The blowing rate (a small effect) is obtained from an assumed heat of ablation of 116 Mj/kg.[15] To this is added the arbitrarily drawn start of a transition criterion line shown on Fig. 3 and tacitly assumed to apply to a smooth vehicle. This is a somewhat artificial way to define transition, but the transition progressions for both the blunt and sharp vehicle cases are representative.

The variation of Re_θ in Fig. 2 shows the sensitivity of calculated transition progression results with respect to the selection of the criterion line. That is, the slopes are nearly equal, so small changes in the criterion would cause large changes in the predicted position of transition at a given altitude. The scatter of the data indicates that transition depends on factors other than Re_θ and shows the difficulty of predicting transition from correlations.

Transition Pattern

Wind tunnel studies using sphere-cone models show that angle of attack and bluntness produce transition pattern asymmetry.[16-20] For pointed cones, transition is promoted on the leeward side and slightly delayed on the windward side. For large bluntness ($r_n/r_b \approx 0.25$) both windward and leeward transition are promoted relative to the side of the body. For intermediate bluntness the front is fairly symmetric, although it moves forward with angle of attack. For a smooth body the pattern is wind fixed, since any skewness remains fixed in relation to the body axis/velocity vector plane. The main effect of pattern skewing is to change the shape of the C_M, C_N vs angle-of-attack curves, i.e., $C_{M\alpha}$ and $C_{N\alpha}$. Incremental force calculations using a wind-tunnel derived pattern skewing model[14] indicate that for low blowing rate heat shields the maximum aerodynamic center shift due to angle of attack less than a few degrees is only about $\pm 0.015L$. This is confirmed by the experiments of Holden.[20] Vehicles normally have a static margin of at least $0.05L$, and for this condition motion simulations[10] indicate negligible dispersion from this mechanism. But this conclusion may not apply to vehicles with higher blowing rate heat shield materials.[19]

Roughness Effect

The inability of wind-fixed pattern skewing to explain the dispersive motions observed for flight vehicles with low blowing rate heat shields requires consideration of other mechanisms. The one investigated in the remainder of this discussion arises from surface roughness. On practical vehicles step and gap dimensions on the order of 0.1-1 mm are common. In addition, re-entry heating causes sufficient ablation to alter the initial surface. The transition pattern behind asymmetric roughness would tend to be body fixed because the roughness is body fixed. But the delay length between the roughness and the start of transition may be strongly influenced by angle of attack and other factors, so the transition pattern due to roughness may not be completely body fixed.

That sudden changes in the body-fixed forces can produce dispersion [see Eq. (3)] suggests the possibility that the sudden appearance or disappearance of "wedges" of turbulence trailing being isolated roughness may be a primary mechanism. Turbulence wedges have been observed on ablating ballistic range models, where the models did not intentionally contain isolated roughness.[21-23] To see how such wedges can be produced and how they may appear or disappear with very small changes in flow conditions, the extensive data base on tripping of the boundary layer in wind tunnels is examined.[24-27] Although the results were obtained mainly on pointed cones containing trip rings consisting of isolated spheres, the recent experiments of Boudreau[28] show that the main effects also apply to blunted cones containing distributed roughness trips. Boudreau's data indicate that distributed roughness may be about four or five times more effective (in terms of roughness height) than a row of spheres and that the most effective location of the roughness is near the pressure minimum on a sphere-cone ($3 < s/r_n < 20$).

Figure 3 illustrates the sensitivity of the start of transition position to roughness near the nose (assumed here at $s/r_n = 4.5$), calculated according to the Potter-Whitfield method.[24-26] Roughness near the nose provides a more effective trip than similar roughness further aft.[14] The smooth wall transition position in Fig. 3 was obtained using the

criterion curve shown in Fig. 2. As the vehicle descends, Fig. 3 suggests that roughness larger than about 0.1 mm may promote early transition. If so, body-fixed turbulence wedges may be formed whenever roughness near the nose is not completely uniform with respect to vehicle meridian. The situation is even more complicated than implied by Fig. 3, since angle of attack is always nonzero (typically, $0<\alpha<1.5$ deg). As the roughness changes from windward to leeward, the transition position behind the roughness could be expected to shift. Any "flashing" on and off of turbulence wedges due to windward/leeward orientation would produce rapid changes in lateral forces and cause dispersion.

Incremental Forces

Despite the difficulty in defining a realistic transition pattern time history, it is instructive to postulate an idealized pattern history to use for example force and motion estimates. The role of isolated roughness in promotion body-fixed force asymmetry is illustrated by calculating the incremental force coefficients at $\alpha=0$ for the example vehicles of Table 1. It is assumed (arbitrarily) that the body has a 1-cm-wide spot of roughness at $s/r_n=4.5$ of height 0.2 mm which acts as a boundary-layer trip, with transition progression behind the trip evaluated by the Potter-Whitfield correlation (see Fig. 3). Wider trips would produce somewhat larger forces. The axial position of the trip is not critical if it is a few nose radii behind the nose.

Because the disturbance from the trip spreads laterally, a wedgelike disturbed region trails the trip. The lateral spreading half-angle of the disturbance and the tripped turbulent flow is obtained from the turbulent spread rate correlation of Fischer.[29] Thus the idealized pattern appears as in Fig. 4, which shows the unrolled cone surface. In the example calculated, the start of transition position of the smooth wall and wedge are obtained from Fig. 3.

The boundary-layer code of Ref. 14 calculates both laminar and turbulent flow along meridians for the wedge and background smooth wall regions, obtains the shear stress and incremental pressure from the displacement effect using a tangent body assumption, and integrates these stresses over the surface to obtain force coefficients. An intermittency factor is used to weight the laminar and turbulent stress values over an assumed intermittency length equal to the streamlength to the start of transition. For this factor, the conical exponential growth model of Chen and Thyson[30] is used. Figure 5 shows the (unweighted) incremental pressure and shear stress at 24 km altitude referred to freestream dynamic pressure $\bar{q}$. Values $\Delta P/\bar{q}\approx 0.002$-$0.008$ are typical for re-entry vehicles, with sharper bodies tending to have higher incremental pressure and shear. Note that the pressure and shear stress increments at any streamwise station depend strongly on the location of transition.

Figure 6 shows the integrated net force and moment with respect to the center of gravity and aerodynamic center for the sphere-cones of Table 1. The shape of the plots may be interpreted using the pattern history of Figs. 3 and 4 and the fact that the induced pressure effect dominates, but the shear stress effect is not negligible. As the vehicle descends, wedge onset occurs first and produces a downward force on the base ($C_{FB}<0$) and a nose-up pitching moment ($C_{MBcg}>0$). The peak in the moment curves around 25 km altitude corresponds to transition onset of the smooth-wall turbulence. As both fronts approach the nosetip, the net force again becomes zero. Generally, the net incremental force acts aft of the aerodynamic center for the blunter body ($C_F<0$, $C_{Mac}>0$). For the sharper body the situation is more complicated.

It should be noted that theoretical force estimates using the above analysis procedure have been verified by unpublished measurements on sphere cones in two hypersonic facilities. In both cases, a turbulence wedge was produced by adding a spot of roughness near the nose. The magnitude of side force due to the wedge (with no background turbulence) was predicted within a few percent. The force center was predicted to be about $0.1L$ ahead of that measured, indicating that the theory is approximate.

Trajectory Response

Despite the idealized nature of the forcing functions, it is interesting to obtain the lateral motion response assuming no feedback effect on forces due to angle of attack. The trajectory parameters of Table 1 are used and the motion is assumed purely ballistic until transition onset. At transition onset (~28 km), K from Eq. (3) is about 2200 m/s, and near the end of transition (~20 km), $K\approx 7900$ m/s. Although the force coefficient histories contain no step changes, rapid changes on the order of $\Delta C_{Mac}\approx 0.0004$ occur. Thus, motion center shifts on the order of 1-3 m/s should be expected for this example.

Figures 7 and 8 show the lateral velocity and angle-of-attack magnitude response to the body-fixed lateral force histories of Fig. 6. (The starting time and initial orientation of the transition forces are arbitrary.) For both example vehicles the net mean ΔV due to transition was about 2 m/s, in line with the rough estimate given in the previous paragraph. If this dispersion was modeled as a discrete event at 25 km altitude, the dispersion normal to the trajectory for path angle

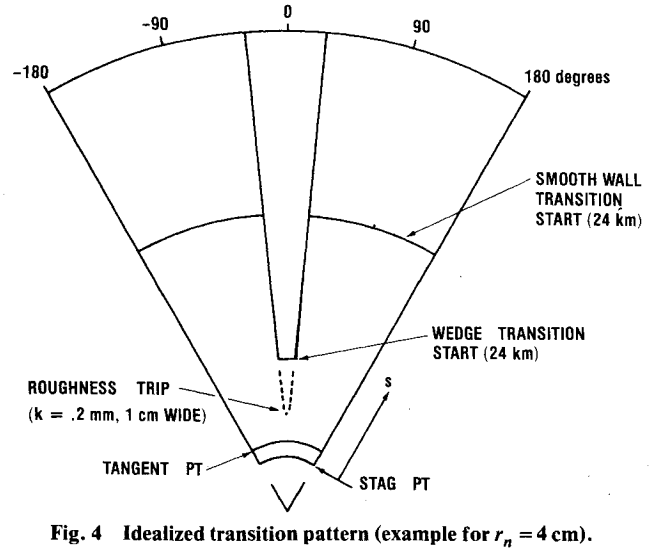

Fig. 4 Idealized transition pattern (example for $r_n=4$ cm).

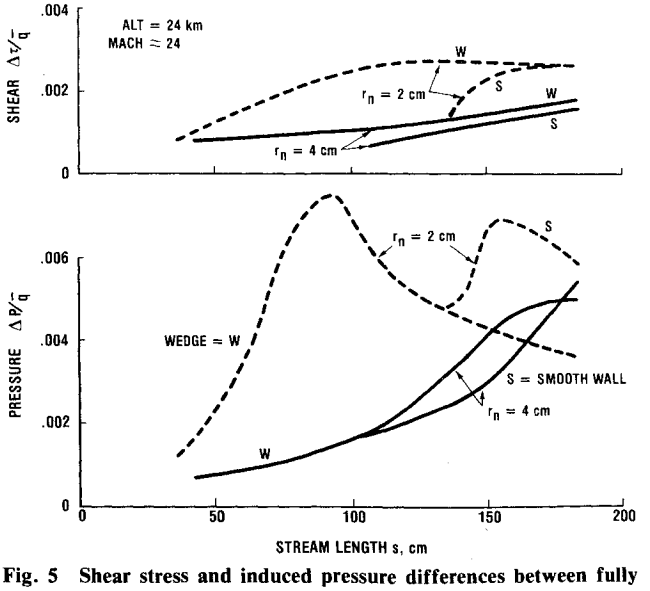

Fig. 5 Shear stress and induced pressure differences between fully turbulent and laminar flow.

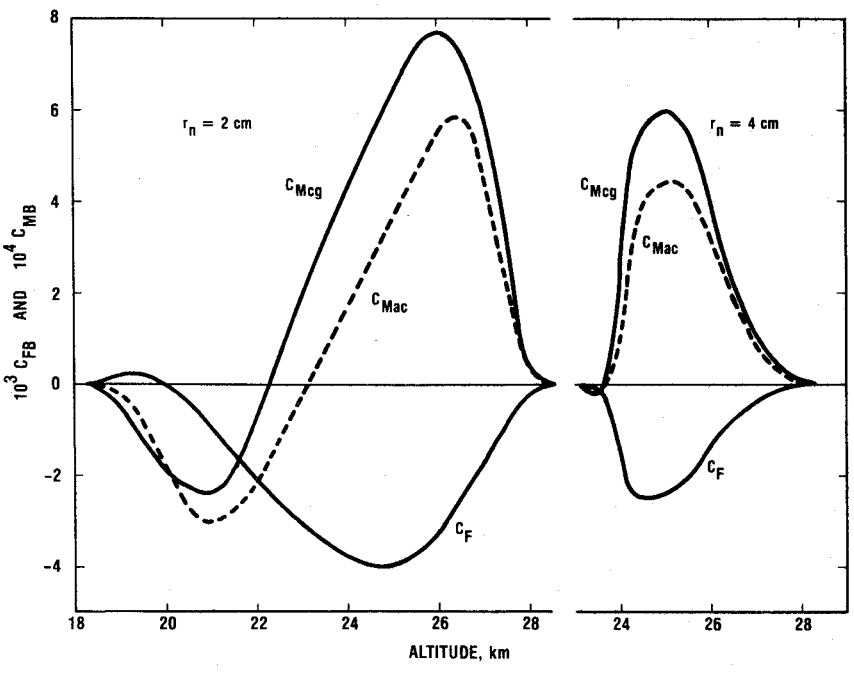

Fig. 6 Force coefficients due to turbulence wedge behind $k=0.2$ mm roughness at $s/r_n=4.5$.

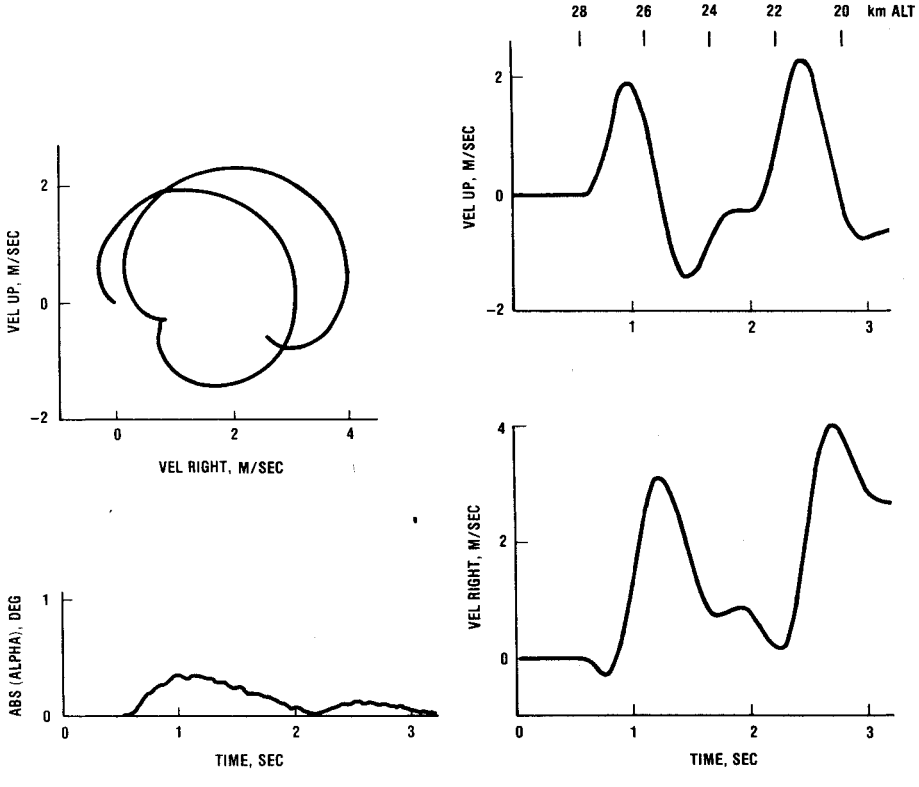

Fig. 7 Motion response ($r_n=2$ cm).

$\gamma=30$ deg would be about 14 m [Eq. (5)]. It should be noted that the total ΔV obtained is a strong function of the roll rate. In addition to the p^{-1} dependence of Eq. (3), the net dispersion obtained depends on what part of the oscillation cycle the vehicle is in when the transition force dies away. Also, realistic transition force histories are expected to be much more "jittery" than those of Fig. 6 due to angle-of-attack effects, and somewhat larger dispersion could occur.

This calculation displays features of what is believed to be the most important frustum transition dispersion mechanism for vehicles like that of Table 1. A precise analysis for an actual vehicle would be considerably more complex. First, a complete specification of the vehicle roughness during transition would be needed. Second, reliable transition correlations to define the start of transition location along each vehicle meridian would be required, including the effects of vehicle orientation. Finally, a boundary-layer analysis would be needed along each meridian to obtain the instantaneous forces. This last item is the most straightforward. Knowledge of the precise vehicle roughness and the transition pattern produced by the roughness remain the greatest uncertainties.

Nosetip Flow Separation

Around 15 km altitude transition moves on to the nosetip and creates an asymmetric pattern that depends on roughness.[3,31] Peak heating rates occur downstream of the sonic point and cause indenting of the tip in the form of

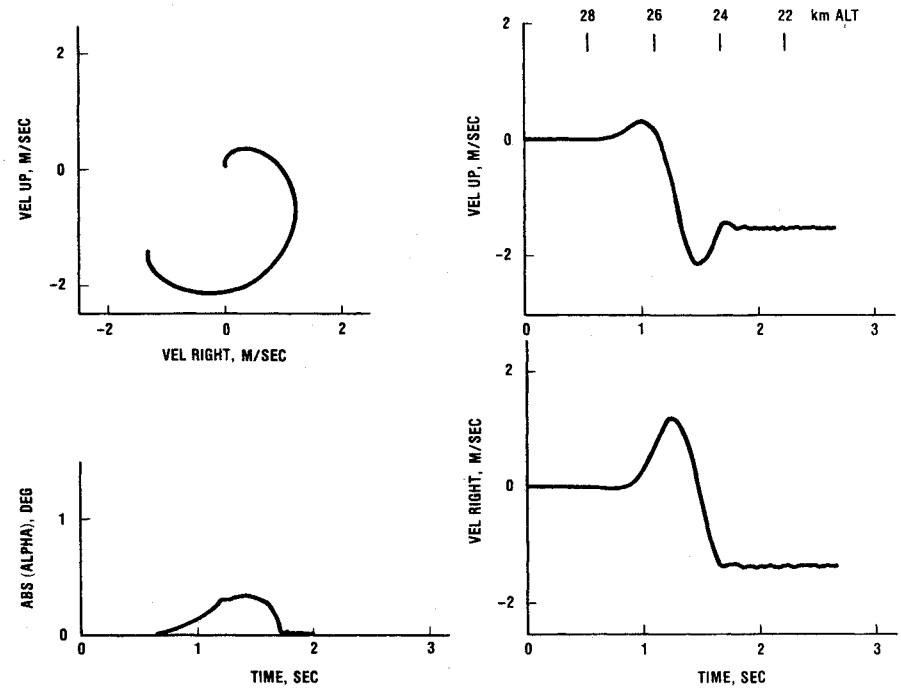

Fig. 8 Motion response ($r_n = 4$ cm).

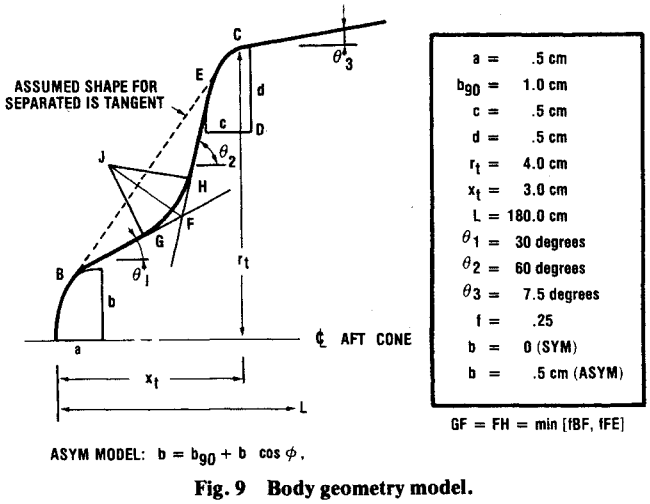

Fig. 9 Body geometry model.

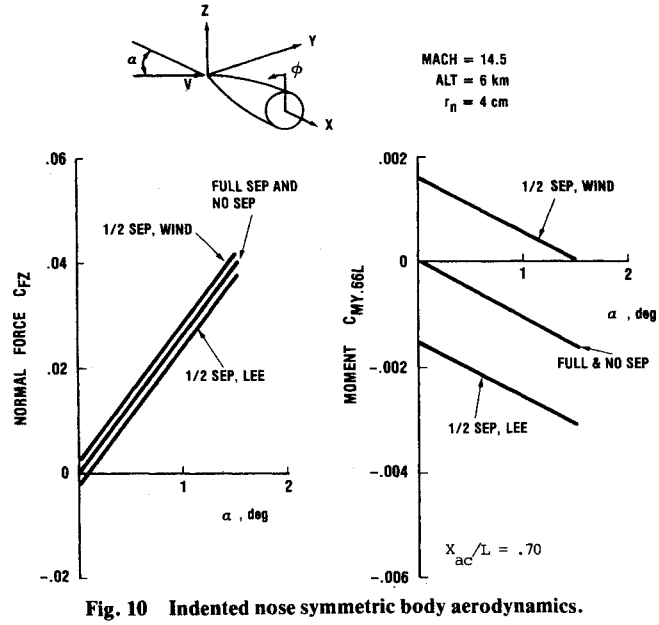

Fig. 10 Indented nose symmetric body aerodynamics.

gouges or scallops.[3,4] If the indenting is severe, flow separation can occur, producing either rapid flowfield oscillations or sudden switches between steady attached and separated flow configurations.[5] This behavior may be a significant dispersion source if it occurs at a high enough altitude and if the associated vehicle lateral force changes are sufficiently large [see Eq. (3)]. The object of this section is to estimate the magnitude of lateral force changes due to nosetip separation to better define the severity of dispersion.

Impulsive Force Change Model

Precise evaluation of asymmetric forces on vehicles with indented tips is difficult because of the complex flowfields associated with boundary-layer separation and imbedded secondary shocks. Here it is assumed that flow separation suddenly changes the shape of the nose essentially by filling in the indented region. The adequacy of this assumption has not been verified experimentally, so the present results are tentative. Figure 9 shows the model and parameters used in the examples. The cross section consists of nose and shoulder ellipses, tangent straight lines, and an equal arc circular fillet in the indented region. An asymmetric shape is generated by allowing the axis b of the nose ellipse to vary with the meridian Φ.

Vehicle force changes are evaluated by integrating the surface pressure distributions obtained from the model used in the ABRES shape change code.[32] In this model the pressure distribution on the conical afterbody is a function of cone angle and nosetip drag coefficient. Separation changes the nose drag, so the afterbody pressures are affected. To calculate forces at angle of attack, a tangent body assumption is made. That is, in each meridian the pressure is calculated for an equivalent axisymmetric body locally tangent to the surface. Thus, the pressure distribution along each meridian is calculated independently and the results are integrated to determine the net vehicle force coefficients.

An attempt was made to evaluate the validity of the force model by comparing calculated results for pressures and force coefficients with representative experimental data. The 50 deg axisymmetric biconic tested by Hahn and Little[33] at Mach 16 is representative of the tangent line separated configuration of Fig. 9. Calculations were compared for this and for several indented shapes tested by Todisco, Zavasky, and Waldman[34]

Table 2 Asymmetric body force coefficients at zero angle of attack for nosetip shown in Fig. 11

Condition	Complete body			Nose only			Base
	C_{FZ}	$C_{MY.66}$	C_X [a]	C_{FZ}	$C_{MY.66}$	C_X [a]	C_X [a]
Attached	.00023	.00039	.0545	.00017	.00010	.0270	−.0063
Sep, upper ½	−.00041	.00123	.0526	.00015	.00005	.0251	−.0065
Sep, lower ½	.00244	.00200	.0563	.00219	.00141	.0286	−.0062
Separated	.00180	.00284	.0544	.00217	.00136	.0268	−.0064

[a] Due to pressure only.

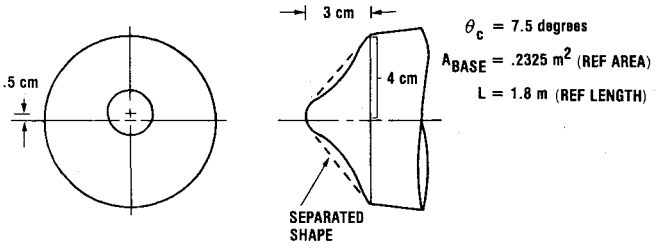

Fig. 11 Typical asymetric nosetip.

at Mach 9. In the cases examined, the normal force slope was within 5% of the data, and aerodynamic center location was within 2% of model length (generally forward of the data). Pressure agreement also was good, except that the measured pressures did not fall as rapidly as predicted behind the body shoulder for the 50 deg biconic. Thus the present theory should be adequate to estimate at least the order of magnitude of lateral force coefficient changes if separation effectively fills in the indented region as assumed.

Symmetric Body

Suppose now that during shape change an incipient separation condition occurs, so with a slight change in shape or angle of attack separation can occur over all or part of the nose. Figure 10 indicates the force coefficients obtained when the symmetric nose of Fig. 9 is applied to the blunt cone of Table 1. Moment coefficient steps up to ±0.0015 can occur due to switches to partially separated flow, either windward or leeward. If this step change occurred at 10 km altitude, the dispersion from Eq. (3) would be ~100 m, using the parameters in Table 1. The switch from fully attached to fully separated flow produces negligible dispersion because axisymmetry is preserved.

Asymmetric Body

A body representative of asymmetric nosetips is obtained using the *b* parameter variation of Fig. 9. Calculations for the complete vehicle using this nose (Fig. 11) are given in Table 2 for partially and fully separated assumptions. The largest moment change of about 0.0025 occurs between the fully attached and fully separated conditions. Once again these moment steps could produce large dispersion if they occur at 5-15 km altitude for a vehicle with a moderate roll rate. Impulsive changes in axial force C_X indicating separation might be detectable in flight data.

Concluding Remarks

This paper attempts to describe the significance to re-entry accuracy of both the frustum transition and nosetip flow separation dispersion mechanisms. For both, deterministic evaluation of dispersion presently is not possible because of the strong dependence on the precise history of transition and nosetip shape change. Thus, the objective of providing a complete design tradeoff procedure has not been realized.

In the case of frustum dispersion, a design approach does exist based on Eq. (3). Frustum dispersion is observed to occur in one or perhaps several jumps. The magnitude of maximum possible moment step can be estimated by postulating worst-case transition pattern asymmetries. It is then necessary that the parameter group K of Eq. (3) be made small enough that ΔV, or Δr in Eq. (5), is acceptably small. If this cannot be done by adjusting roll rate and static margin, then additional roughness can be added near the nosetip to raise the transition altitude to reduce the density during transition. The penalty for this is the slightly increased heat shield weight needed to provide for the additional turbulent heating rates encountered.

Nosetip flow separation can cause serious dispersion if the lateral moment coefficient change is large or the distance to impact is great. One design approach to alleviate the problem is the "shape stable nosetip" concept,[35] in which the central portion of the tip is made of material with less resistance to ablation than the outer annulus. The idea is to prevent the indented proboscidean shape from developing, prevent separation, and keep the tip more nearly axisymmetric. Whether or not this concept is used, further analysis of dispersion from indented nosetips requires development of criteria for predicting incipient separation and on better quantifying the resulting lateral forces.

Acknowledgments

This work was sponsored by the USAF Space and Missile Systems Organization under Contracts F04701-76-C-0069 and F04701-77-C-0130.

References

[1] Glover, L.S., "Approximate Equations for Impact Dispersion Resulting From Winds and Deviations in Density," *Journal of Spacecraft and Rockets,* Vol. 9, July 1972, pp. 483-484.

[2] Chrusciel, G.T., "Analysis of Re-Entry Vehicle Behavior During Boundary-Layer Transition," *AIAA Journal,* Vol. 13, Feb. 1975, pp. 154-159.

[3] Dirling, R.B., Jr., "Asymmetric Nose-Tip Shape Change During Atmospheric Entry," *Aerodynamic Heating and Thermal Protection Systems,* Vol. 59, *Progress in Astronautics and Aeronautics,* edited by L.S. Fletcher, AIAA, New York, 1978, pp. 311-327.

[4] Derbidge, T.C., Wool, M.R., Morse, H.L., and Overly, P.T., "Definition of Shape Change Phenomenology From Low Temperature Ablator Experiments—Part III, Shape Change Data Correlation and Analysis," Acurex Corporation, Mountain View, Calif., SAMSO-TR-74-86, Vol. 5, Jan. 1974.

[5] Abbett, M.J., Cooper, L., Dahm, T.J., and Jackson, M.D., "Flow Characteristics About Concave Conic Forebodies at High Mach Numbers," AIAA Paper 75-153, Jan. 1975.

[6] Kryvoruka, J.K., Bramlette, T.T., "Effect of Ablation-Induced Roll Torques on Reentry Vehicles," *Journal of Spacecraft and Rockets,* Vol. 14, June 1977, pp. 370-375.

[7] Platus, D.H., "Dispersion of Spinning Missiles Due to Lift Nonaveraging," *AIAA Journal,* Vol. 15, July 1977, pp. 909-915.

[8] Crenshaw, J.P., "Effect of Lift Variation on the Impact of a Rolling Reentry Vehicle," *Journal of Spacecraft and Rockets,* Vol. 9, April 1972, pp. 284-286.

[9] Etkin, B., *Dynamics of Flight,* John Wiley & Sons, New York, 1959, Chap. 13.

[10] King, H.H., "Phenomenology of High Altitude Dispersion," Effects Technology, Inc., Santa Barbara, Calif., SAMSO-TR-77-90, Vol. XI, Sept. 1977.

[11] Morrison, A.M., Solomon, J.M., Ciment, M., and Ferguson, R.E., "Handbook of Inviscid Sphere-Cone Flow Fields and Pressure Distributions," Vol. II, Naval Surface Weapons Center, Silver Spring, Md., Dec. 1975.

[12] Fisher, L.R., "Equations and Charts for Determining the Hypersonic Stability Derivatives of Combinations of Cone Frustums Computed by Newtonian Impact Theory," NASA TN D-149, Nov. 1959.

[13] Berkowitz, A.M., Kyriss, C.L., and Martellucci, A., "Boundary Layer Transition Flight Test Observations," AIAA Paper 77-125, Jan. 1977.

[14] King, H.H., "Incremental Forces From Boundary Layer Transition," Effects Technology, Inc., Santa Barbara, Calif., SAMSO-TR-77-90, Vol. VI, Aug. 1977.

[15] Minges, M.L., "Ablation Phenomenology (A Review)," *High Temperatures-High Pressures,* Vol. 1, 1969, pp. 607-649.

[16] Stetson, K.F. and Rushton, G.H., "Shock Tunnel Investigation of Boundary-Layer Transition at $M=5.5$," *AIAA Journal,* Vol. 5, May 1967, pp. 899-906.

[17] Marvin, J.G. and Akin, C.M., "Combined Effects of Mass Addition and Nose Bluntness on Boundary-Layer Transition," *AIAA Journal,* Vol. 8, May 1970, pp. 857-863.

[18] DiCristina, V., "Three-Dimensional Boundary-Layer Transition on a Sharp 8° Cone at Mach 10," *AIAA Journal,* Vol. 8, May 1970, pp. 852-856.

[19] Martellucci, A., "Asymmetric Transition Effects on the Static Stability and Motion History of a Slender Vehicle," General Electric, Philadelphia, Pa., SAMSO-TR-70-141, Jan. 1970.

[20] Holden, M.S., "Studies of the Effects of Transitional and Turbulent Boundary Layers on the Aerodynamic Performance of Hypersonic Re-Entry Vehicles in High Reynolds Number Flows," Calspan Corp., Buffalo, N.Y., AB-5384-A-2, Dec. 1978.

[21] Wilkins, M.E., "Evidence of Surface Waves and Spreading of Turbulence on Ablating Models," *AIAA Journal,* Vol. 3, Oct. 1965, pp. 1963-1965.

[22] Wilkins, M.E. and Tauber, M.E., "Boundary-Layer Transition on Ablating Cones at Speeds up to 7 km/sec," *AIAA Journal,* Vol. 4, Aug. 1966, pp. 1344-1348.

[23] Canning, T.N., Wilkins, M.E., and Tauber, M.E., "Ablation Patterns on Cones Having Laminar and Turbulent Flows," *AIAA Journal,* Vol. 6, Jan. 1968, pp. 174-175.

[24] Potter, J.L. and Whitfield, J.D., "Effects of Slight Nose Bluntness and Roughness on Boundary Layer Transition in Supersonic Flows," *Journal of Fluid Mechanics,* Vol. 12, 1962, pp. 501-535.

[25] Whitfield, J.D., Ianuzzi, F.A., "Experiments on Roughness Effects on Cone Boundary-Layer Transition Up to Mach 16," *AIAA Journal,* Vol. 7, March 1969, pp. 465-469.

[26] Pate, S.R., "Supersonic Boundary Layer Transition: Effects of Roughness and Freestream Disturbances," *AIAA Journal,* Vol. 9, May 1971, pp. 797-803.

[27] van Driest, E.R. and Blumer, C.B., "Boundary Layer Transition at Supersonic Speeds: Roughness Effects with Heat Transfer," *AIAA Journal,* Vol. 6, April 1968, pp. 603-607.

[28] Boudreau, A.H., "Artificially Induced Boundary-Layer Transition on Blunt-Slender Cones Using Distributed Roughness and Spherical-Type Tripping Devices at Hypersonic Speeds," Arnold Air Force Station, Tenn., AEDC-TR-77-120, Feb. 1978.

[29] Fischer, M.C., "Spreading of a Turbulent Disturbance," *AIAA Journal,* Vol. 10, July 1972, pp. 957-959.

[30] Chen, K.K. and Thyson, N.A., "Extension of Emmons' Spot Theory to Flows on Blunt Bodies," *AIAA Journal,* Vol. 5, May 1971, pp. 821-825.

[31] Anderson, A.D., "Boundary Layer Transition on Nosetips with Rough Surfaces," Acurex Corp., Mountain View, Calif., SAMSO-TR-74-86, Vol. 10, edited by M.R. Wool, Jan. 1975.

[32] Dahm, T.J., Cooper, L., Rafinejad, D., Youngblood, S.B., and Kelly, T.J., "Inviscid Flow and Heat Transfer Modeling for Reentry Vehicle Nosetips," Acurex Corp., Mountain View, Calif., SAMSO-TR-77-11, Vol. 1, Oct. 1976.

[33] Hahn, J.S. and Little, H.R., "Force and Pressure Tests on Cones with Simulated Ablated Noses at Mach Numbers 8 and 16," Arnolds Air Force Station, Tenn., AEDC-TR-72-52, April 1972.

[34] Todisco, A., Zavasky, J. and Waldman, G., "Irregular Nosetip Shape Pressure and Force," Avco Systems, Wilmington, Mass., SAMSO-TR-75-269, Vol. 11, Aug. 1976.

[35] Holtz, T., Derbidge, T.C. and Sandhu, S.S., "Low Temperature Ablator Experiments on Shape Change Technology (Series K) and Shape Stable Nosetip Design (Series L)," Acurex Corp., Mountain View, Calif., TM-76-128, Aug. 1976.